Available online at www.sciencedirect.com
SCIENCE DIRECT®
ELSEVIER
Journal of Non-Crystalline Solids 316 (2003) 261–272
JOURNAL OF NON-CRYSTALLINE SOLIDS
www.elsevier.com/locate/jnoncrysol

# The structure and properties of binary zinc phosphate glasses studied by molecular dynamics simulations

B.C. Tischendorf [a], T.M. Alam [b], R.T. Cygan [c], J.U. Otaigbe [a,*]

[a] *Department of Materials Science and Engineering, Iowa State University, Gilman Hall, Ames, IA 50011, USA*
[b] *Department of Organic Materials, Sandia National Laboratories, Albuquerque, NM 87185, USA*
[c] *Department of Geochemistry, Sandia National Laboratories, Albuquerque, NM 87185, USA*

Received 26 November 2001; received in revised form 23 May 2002

**Abstract**

In recent years, the use of molecular dynamics (MD) simulations to understand and predict the properties of materials has become an increasingly popular and powerful tool. In this study, MD simulations were used to investigate the structural and physical properties of a binary zinc phosphate glass series, $x\mathrm{ZnO}\cdot(100-x)\mathrm{P_2O_5}$, $(40\leqslant x\leqslant 70)$ where $x$ is the mole percent modifier. A newly developed forcefield model incorporating Coulombic, plus two- and three-body interactions was employed, with the model parameters being empirically derived from known zinc–phosphate crystal structures. This zinc–phosphate forcefield model was used to perform MD calculations of densities, glass transition temperatures, $T_g$, average coordination numbers (CN) radial distribution functions, $G(r)$, and pair distribution function, $g(r)$, as a function of Zn concentration. In addition, the effects of computational quenching rates on the simulated densities were also investigated. Overall, the MD simulation results revealed the presence of long-range order in the form of rings and chains near the metaphosphate composition. These extended range structures disappeared beyond the metaphosphate composition, becoming isolated non-bridging phosphate tetrahedron as the Zn concentration approached the pyrophosphate composition. The MD simulations also revealed that the average Zn CN was invariant across the entire Zn concentration range investigated. These results demonstrate that the observed $T_g$ behavior does not require an increase in the Zn CN.


## 1. Introduction

There is considerable interest in determining the local and extended range structure of zinc polyphosphate glasses. They exhibit higher durability, lower glass transition temperatures ($T_g$) and a wide glass-forming composition range when compared to other common phosphate glass systems [1–4]. Zinc polyphosphate glasses are used in a number of technologically important applications, including the manufacturing of glass-polymer composites, optical waveguides, and solid-state laser sources [5,6]. Because zinc phosphate glasses have thermal expansion coefficients similar to that of many metals, they are also used as seals and welds between glassy and metallic parts.

* Corresponding author. Present address: School of Polymers and High Performance Materials, University of Southern Mississippi, Box 10076, Hattiesburg, MS 39406-0076, USA. Tel.: +1-601 266 5596; fax: +1-601 266 5504.
*E-mail address:* joshua.otaigbe@usm.edu (J.U. Otaigbe).

0022-3093/03/$ - see front matter 
PII: S0022-3093(02)01795-7

Techniques used to study phosphate glass structure include X-ray diffraction [7–9], X-ray photoelectron spectroscopy [10,11], extended X-ray absorption fine structure [12], Raman spectroscopy [13,14], infrared spectroscopy [14], and nuclear magnetic resonance (NMR) [13–17]. More recently, as the quality and reliability of interaction forcefields have improved, along with the increases in computation speed, molecular dynamics (MD) simulations have become an important and inexpensive tool to study the relationships between glass structure and the measured physical properties [18–33].

Previous MD studies of glass systems have involved the use of two-body potentials expressed in a variety of analytical forms [21,22,31,32]. These studies have been able to predict the structure and density in glass systems, but have had great difficulty in the prediction of $T_g$, especially in phosphate systems due to the anisotropy of the phosphate bonding environment. Previous MD simulations of phosphate glass systems have been reported for $NaPO_3$ [32], $Mg(PO_3)_2$, $Zn(PO_3)_2$ and $Pb(PO_3)_2$ glasses [22,31], the $x\mathrm{CaO}\cdot(100-x)\mathrm{P_2O_5}$ [34], $x\mathrm{Li_2O}\cdot(100-x)\mathrm{P_2O_5}$ [24], $50\mathrm{Na_2O}\cdot x\mathrm{Al_2O_3}\cdot(50-x)\mathrm{P_2O_5}$, and $(50-x/2)\mathrm{Na_2O}\cdot x\,\mathrm{Al_2O_3}\cdot(50-x/2)\mathrm{P_2O_5}$ glass series [35]. Only the MD simulations by Liang et al. for the ultraphosphate $x\mathrm{Li_2O}\cdot(100-x)\mathrm{P_2O_5}$ glass series attempted to determine the $T_g$ behavior directly from the MD simulations [24].

It has also recently been shown that the use of two-body potentials in conjunction with a series of three-body (angle bending) interaction potentials for the MD forcefield allows for a more accurate representation of the phosphate glass structure and properties [18,24]. In this manuscript, these newly developed three-body forcefield models were extended to perform MD simulations for a series of binary zinc phosphate glasses. Changes in the simulated structural details as a function of Zn concentration are quantified and correlated with the simulated changes in density and $T_g$ behavior. It is hoped that the development of these multi-body forcefield models will eventually allow for the simulation of the physical properties and long-range structural order in significantly more complex glass systems.

## 2. Computational details

### 2.1. Development of the forcefield model

The reliability of any MD simulation is directly related to the quality of the energy forcefield model used to describe the interatomic interactions. The majority of previous MD simulations of glasses have relied almost exclusively on two-body interaction potentials. The presence of P–O bonding anisotropy in phosphate systems, including the presence of bridging P–O–P, non-bridging $P–O^-$, and terminal P=O bonding configurations, results in significant inaccuracies for MD simulations that utilize models containing only two-body interactions [24]. To improve the accuracy of the simulated phosphate glass structure, a previously reported forcefield model containing a combination of two- and three-body interaction potentials was used in the present study [24]. Two separate interaction terms were used to describe the short-range two-body interactions. In addition to the standard Coulombic (electrostatic) interactions, a Lennard-Jones (LJ) potential energy function (Eq. (1)) was used:

$$E_{\mathrm{LJ}} = D_0\left[\left(\frac{r_0}{r}\right)^{12} - 2\left(\frac{r_0}{r}\right)^{6}\right], \tag{1}$$

where $D_0$ and $r_0$ are adjustable parameters, and $r$ represents the interatomic distance. For the LJ potential only cation–anion and anion–anion interactions make significant contribution to the overall energy, and therefore are the only LJ interactions explicitly evaluated. The three-body energy terms in the model describe the O–P–O and P–O–P interactions, and are used to constrain the tetrahedral angles within the $PO_4$ tetrahedra. The three-body interaction potential is defined by

$$E_{\mathrm{angle}} = \frac{k_0}{2}(\theta-\theta_0)^2, \tag{2}$$

where $\theta$ is either the O–P–O or P–O–P bond angle, and $\theta_0$ and $k_0$ are adjustable parameters. For the O–P–O interaction $\theta_0$ is fixed to the equilibrium tetrahedral angle of 109.47°.

The parameters in Eqs. (1) and (2) were determined using known crystal structures of $P_2O_5$ [36–

38] as well as zinc phosphate crystal structures [8,39–45]. The P and O interactions were empirically parameterized based on three crystalline forms of $P_2O_5$ as has been previously described [24]. The Zn–O interactions were parameterized using the following four zinc phosphate crystal structures [8,39–41]:

(a) The α zinc orthophosphate structure, $Zn_3(PO_4)_2$, with monoclinic space group C2/c. It consists of spiral chains of alternating phosphate and zinc tetrahedron running parallel to the twofold screw axis. These chains are then interconnected by a second set of zinc tetrahedral.

(b) The γ zinc orthophosphate, $Zn_3(PO_4)_2$, with monoclinic space group $P_1^2/c$. It consists of sheets of coordinated cation polyhedra with pairs of tetrahedrally coordinated cations separated by octahedrally coordinated Zn atoms. Phosphate atoms bridge the sheets sharing three oxygen with one sheet and a single oxygen with the adjacent sheet.

(c) The zinc polyphosphate (metaphosphate), $Zn(PO_3)_2$, with monoclinic space group C2/c. It consists of sheets of four member rings of phosphate anions connected to octahedral zinc atoms with a second type of octahedral zinc present in chains interconnecting the sheets.

(d) The zinc ultraphosphate, $ZnP_4O_{11}$, with monoclinic space group $P12_1/c1$. It consists of 'infinite' sheets of phosphate anions (regarded either as interconnected rings or chains), which are interconnected by octahedral zinc atoms.

These four crystal structures and the General Utility Lattice Program (GULP [46]) were used to parameterize the LJ and three-body values noted above. In order to obtain accurate results for the Coulombic component of the molecular model, partial charges were used in place of formal charges. These partial charges were determined both from the work of Uchino and Yoko [33] as well as from our own density functional calculations. The resulting parameters for the forcefield model are given in Table 1. Using these parameters, a solid solution series of six binary zinc glass compositions having compositions $x\mathrm{ZnO}\cdot(100-x)\mathrm{P_2O_5}$, $(40 \leqslant x \leqslant 70)$ were constructed and subsequently studied.

Table 1
Empirical forcefield parameters[a]

| | $D_0$ (eV) | $r_0$ (nm) |
|---|---|---|
| *Two-body interactions* | | |
| $P^{1.85}$–$O^{-0.74}$ | 0.004251 | 0.21550 |
| $O^{-0.74}$–$O^{-0.74}$ | 0.012185 | 0.32743 |
| $Zn^{0.74}$–$O^{-0.74}$ | 0.000827 | 0.31343 |
| | $k_0$ (eV/rad$^2$) | $\theta_0$ (°) |
| *Three-body interactions* | | |
| O–P–O | 3.5401 | 109.47 |
| P–O–P | 20.9326 | 135.58 |

[a] See text for definition of symbols and parameters.

## 2.2. MD simulations

MD simulations were performed within the Cerius-2 software and the open forcefield energy program [47]. For any composition in the series an orthogonal unit cell containing between 500 and 525 atoms was used. Details of the initial cell parameters are given in Table 2, based on experimentally determined target densities. After construction of the unit cell, the positions of the atoms were randomized to reduce the possibility of the initial starting position influencing the final quenched structure. A set of simulations where the atoms types were originally clustered was also performed to demonstrate that the high temperature melt was sufficient to remove any effects of the original configuration (data not shown). The MD simulations of the simulation cell utilized periodic boundary conditions to prevent edge effects. The total energy of the box was then minimized using the forcefield description of the energy while simultaneously recalculating the atomic bonding

Table 2
Properties of the cells used for the MD simulations of the zinc phosphate glasses, $x\mathrm{ZnO}\cdot(100-x)\mathrm{P_2O_5}$

| Composition | Total # of atoms | Starting density (g/cm$^3$) | Cell dimensions $x = y = z$ (nm) |
|---|---|---|---|
| $40.0\mathrm{ZnO}\cdot60.0\mathrm{P_2O_5}$ | 500 | 2.80 | 19.113 |
| $50.0\mathrm{ZnO}\cdot40.0\mathrm{P_2O_5}$ | 525 | 2.85 | 19.910 |
| $55.0\mathrm{ZnO}\cdot45.0\mathrm{P_2O_5}$ | 509 | 3.05 | 19.226 |
| $60.0\mathrm{ZnO}\cdot40.0\mathrm{P_2O_5}$ | 500 | 3.30 | 18.798 |
| $65.0\mathrm{ZnO}\cdot35.0\mathrm{P_2O_5}$ | 525 | 3.48 | 18.994 |
| $70.0\mathrm{ZnO}\cdot30.0\mathrm{P_2O_5}$ | 525 | 4.01 | 18.370 |

throughout the calculation to ensure proper evaluation of the three-body energy terms.

The simulation cells were then equilibrated at 3000 K using a constant volume and temperature (NVT) canonical ensemble, with the temperature of the simulation cell being maintained using the Hoover scheme. The cell temperature was maintained at 3000 K to achieve active melting for 50 ps, with the Newtonian equations of motion recalculated in 1 fs time steps. This produced a total of 50 000 time steps at this temperature, with the atomic connectivities recalculated every 10 steps (10 fs) to allow for the breaking and reforming of the bonds. After the atomic connectivities were determined (10 fs steps) the two- and three-body potentials were re-evaluated for the new bonding environment. Following the initial 50 ps high temperature (3000 K) melting simulation, the system was quenched in 500 K steps to 300 K with an equilibration of 7 ps at each step. The final temperature step was from 500 to 300 K. This quenching scheme corresponds to a cooling rate of approximately $7 \times 10^{11}$ K/s. In addition, MD simulations were also performed with 250 and 125 K steps during the quench, corresponding to a effective quench rates of $3.5 \times 10^{11}$ and $1.75 \times 10^{11}$ K/s, respectively. When the temperature of the simulation cell had been quenched to 300 K, it was then equilibrated for an additional 100 ps under constant pressure temperature conditions (NPT) to ensure that the simulation cell was stable and to allow the atoms to reach a final equilibrium configuration.

### 2.3. Determination of the glass transition temperature, $T_g$

The glass transition temperature of the simulation cell can be found by monitoring the change in the slope of the molar volume versus temperature ($V$–$T$) relation that occurs as a result of the $T_g$ transition while maintaining a constant pressure. The $T_g$ simulation procedure is the computational analog to the experimental determination of $T_g$ using dilatometry. Determination of this relationship is accomplished through heating the simulation cell in a series of small temperature steps as an NPT ensemble and allowing for a 50 ps equilibration at each step. At the end of each temperature step the density or molar volume of the box is calculated. By plotting the change in the molar volume as a function of temperature, and then performing linear regressions for the data on each side of the transition, the intersection of the regression lines allowed the determination of $T_g$. An example of the resulting $V$–$T$ curve and corresponding regression is shown in Fig. 1 for the 65 mol% Zn phosphate glass.

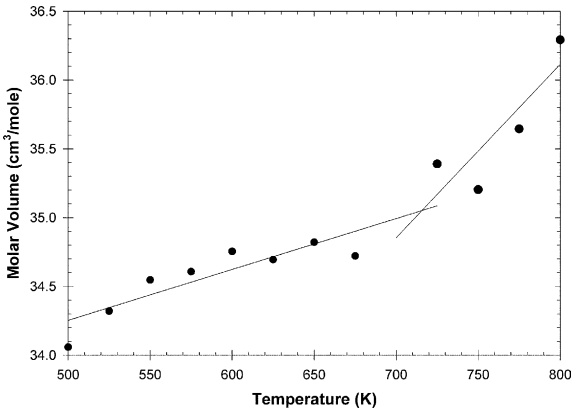


Fig. 1. Molar volume of a simulation cell as a function of temperature. Linear regressions on the two regions provide an intersection that is the glass transition temperature of the system.

## 3. Results

The energy forcefield obtained for the P–O, O–O, P–O–P and O–P–O interactions have previously been reported for the lithium ultraphosphate glass series [24]. The Zn–O interaction parameters (Table 1) are the only new parameters required for the MD simulations described here. The forcefield parameters for the $Zn^{0.74}$–$O^{-0.74}$ (partial charges noted as superscript) LJ potential (Eq. (1)) produce a slightly longer equilibrium Zn–O bond length, and a greater potential well depth than those for the $Li^{0.37}$–$O^{-0.74}$ forcefield parameters previously described [24].

### 3.1. MD simulations of densities

Using the forcefield and simulation procedures detailed above, the densities obtained from the

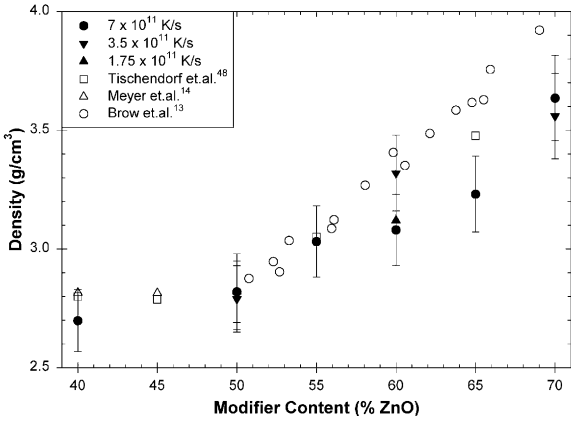


Fig. 2. Comparison of the density of the simulation cells to those of published data. There are two data points at $x = 60$ one for each of two different cooling rates explained in the discussion. Error bars are ±5% based on prior studies of quench rate effects on data shown [50].

MD simulations are shown in Fig. 2, along with the experimental densities available from different sources [13,14,48]. While the density is an initial input parameter for the construction of the MD simulation cells, the final 100 ps NPT equilibration allows the density to change in order to equilibrate the total energy of the simulation cell. As seen in Fig. 2, the calculated densities agree well with the experimental values. In particular the abrupt increase in the glass density above the metaphosphate composition ($x = 50\%$), along with the constant density below the metaphosphate composition, is reproduced. The atomic structural changes that may be responsible for this sudden increase in density will be discussed later.

### 3.2. The effect of quench rate on densities

To address whether changes in the quench rate could reduce the deviations between MD simulated and experimental density at the higher metal concentrations in the zinc phosphate glasses, MD simulations for up to three different quench rates for selected compositions were performed. The results are shown in Table 3. As can be seen in Table 3 and Fig. 2, the lowering of the quench rate does seem to allow for the density to become closer to that of the experimental glass systems. Additionally, the metaphosphate simulation does not appear to overshoot the density.

Table 3
Effect of MD simulation quench rate on the calculated density

| Composition (mol% ZnO) | Experimental density (g/cm$^3$) | Simulated density (g/cm$^3$) | | |
|---|---|---|---|---|
| | | Quench rate 1 ($7 \times 10^{11}$ K/s) | Quench rate 2 ($3.5 \times 10^{11}$ K/s) | Quench rate 3 ($1.75 \times 10^{11}$ K/s) |
| 40 | 2.81 | 2.70 | – | – |
| 50 | 2.83 | 2.82 | 2.79 | 2.82 |
| 55 | 3.06 | 3.03 | – | – |
| 60 | 3.39 | 3.08 | 3.32 | 3.12 |
| 65 | 3.55 | 3.23 | – | – |
| 70 | 4.03 | 3.64 | 3.56 | – |

Standard deviation for the calculations is 0.02 g/cm$^3$.

### 3.3. MD simulations of the glass transition temperature ($T_g$)

The calculated glass transition temperatures obtained from the MD simulations as a function of mole percent Zn are shown in Fig. 3. The agreement with previous experimental evaluation is very good. The minimum in the $T_g$ near the metaphosphate composition (~60 mol%) is reproduced very well by the MD simulation results. The values at the low and high end of the compositional range deviate slightly to higher temperatures than the experimental values.

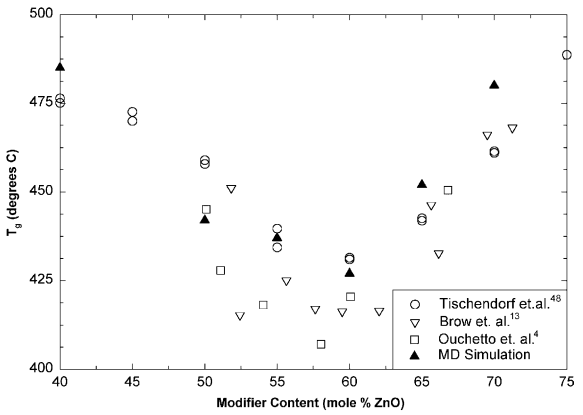


Fig. 3. Experimental $T_g$ values from literature and those determined from the MD simulations as a function of the glass composition.

### 3.4. Short-range structure of the Zn phosphate glass series $xZnO \cdot (100 - x)P_2O_5$

The MD simulations allow the radial distribution function, $G(r)$, to be easily evaluated. The individual pair distribution functions, $g(r)$, for the different pairs of nuclei for each simulation can also be readily determined as shown in Fig. 4 for the metaphosphate composition. In the total $G(r)$ the shorter interatomic distances are well-resolved allowing evaluation of changes in the short-range structure via changes in the P–O, Zn–O and O–O distances. At greater interatomic distances many of these different $g(r)$ curves overlap, obscuring medium range and long structural changes from a simple evaluation of the total $G(r)$. One major difficulty in MD simulations of glasses and amorphous structures is the lack of detailed experimental information to verify the accuracy of the structural model. For Zn phosphate glasses there are very few published neutron diffraction results. Only data for the Zn metaphosphate glass has been reported, allowing a comparison between the simulated and experimental $G(r)$ as shown in Fig. 5(a) [19,49]. In addition, a comparison of $G(r)$ extracted from unpublished neutron diffraction data for the 60 and 70 mol% Zn phosphate glass is shown in Fig. 5(b) and (c) [49].

Fig. 6 shows the variation of the MD simulated radial distribution function $G(r)$, as a function of Zn concentration for the $x\mathrm{ZnO} \cdot (100 - x)\mathrm{P_2O_5}$

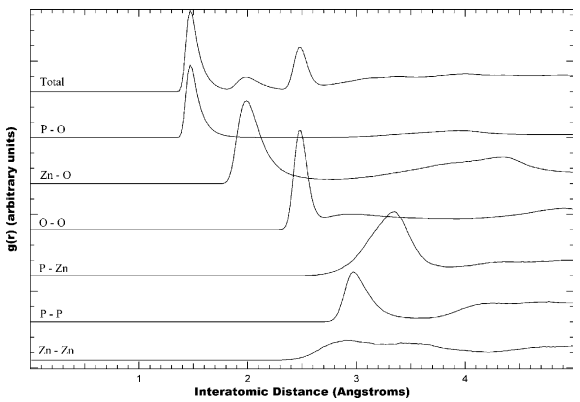


Fig. 4. Calculated individual radial pair distribution functions for the metaphosphate composition.

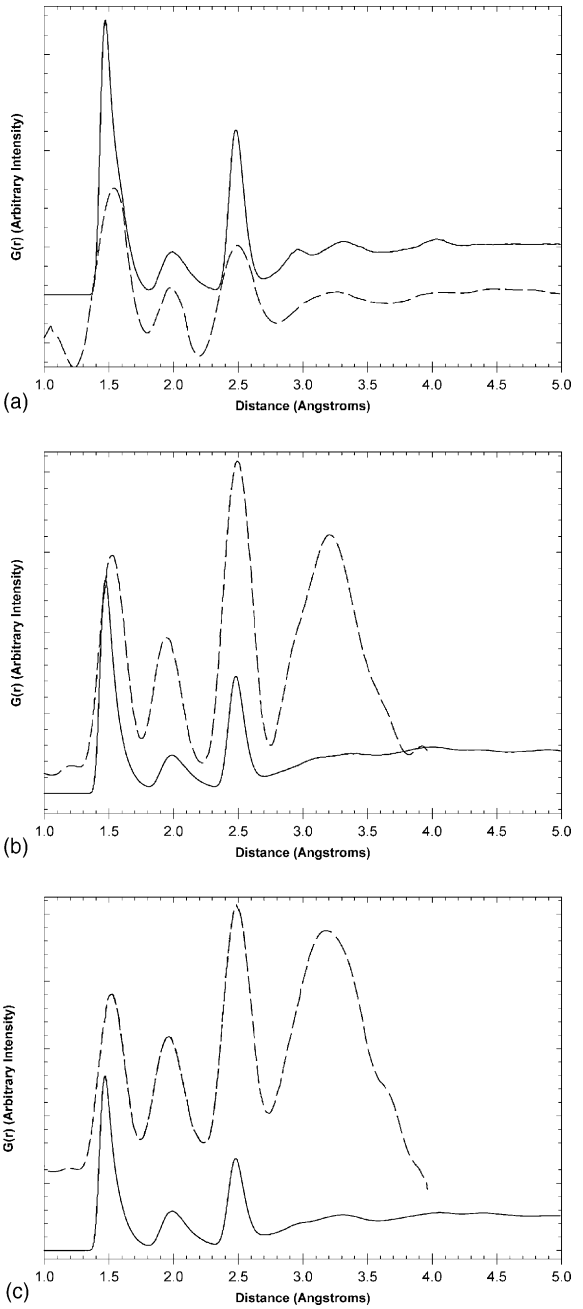


Fig. 5. Radial distribution functions of the equilibrated MD simulations from this work compared to previously published data and unpublished results for the glass compositions of (a) $x = 50$ [19], (b) $x = 55$ [49], and (c) $x = 60$ [49] mol% ZnO. In all graphs the solid line is the simulation data and the dotted line is the experimental data offset for easier comparison.

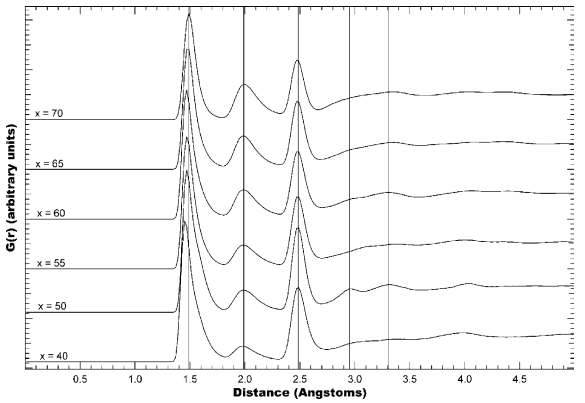


Fig. 6. Calculated radial distribution functions as a function of interatomic distance for the series of glass compositions studied.

glass series. Small changes in $G(r)$ are observed. The P–O, Zn–O, and P–Zn interatomic distances all show a minimal decrease with increasing zinc concentration (see Table 4). Only the $x = 50$ mol% simulation shows a distinction between the Zn–P and the P–P interatomic distances, an anomaly noted during the multiple MD simulations for this concentration. There is no explanation for this behavior at present, but may involve some stabilization to a more crystalline-like structure as the metaphosphate crystal structure, $Zn(PO_3)_2$, is a strong crystal-forming composition, and was used in the initial forcefield parameterization (see Section 2.1).

Changes in the average Zn coordination environment were also evaluated. The average Zn coordination number (CN) and the average O–Zn–O bond angle are given in Table 5. The distribution of the CN as a function of Zn concentration is shown in Fig. 7. The MD simulations clearly show that the average Zn coordination environment is invariant to changes in the Zn concentration. While there is no significant change in the CN distribution with increasing Zn concentration, it should be noted that Zn atoms having CN = 3, 4 and 5 are observed in significant amounts during the simulations.

Table 4
Interatomic distances derived from the pair distribution functions in $x\mathrm{ZnO}\cdot(100-x)\mathrm{P_2O_5}$ glass series

| Composition (mol% ZnO) | First peak (Å) | | | |
|---|---|---|---|---|
| | P–O (Å) | Zn–O (Å) | O–O (Å) | P–Zn (Å) |
| 50 | 1.49 | 1.99 | 2.47 | 3.35 |
| 55 | 1.48 | 1.99 | 2.47 | 3.35 |
| 60 | 1.47 | 1.99 | 2.48 | 3.31 |
| 65 | 1.47 | 1.98 | 2.48 | 3.31 |
| 70 | 1.47 | 1.98 | 2.48 | 3.31 |

Table 5
Average CNs and average angle distributions derived from the pair distribution functions in the $x\mathrm{ZnO}\cdot(100-x)\mathrm{P_2O_5}$ glass series

| Composition (mol% ZnO) | CN[a] | | | ⟨O–Zn–O⟩[b] |
|---|---|---|---|---|
| | Zn–O (2.5 Å) | Zn–P (4.0 Å) | P–Zn (4.0 Å) | |
| 40 | $3.8\pm0.5$ | $4.6\pm0.9$ | $1.9\pm0.8$ | 108 |
| 50 | $3.7\pm0.7$ | $4.8\pm0.8$ | $2.4\pm1.1$ | 108 |
| 55 | $3.9\pm0.7$ | $4.7\pm0.7$ | $2.9\pm1.1$ | 108 |
| 60 | $3.9\pm0.8$ | $4.6\pm0.9$ | $3.5\pm1.3$ | 108 |
| 65 | $4.0\pm0.7$ | $4.4\pm0.9$ | $4.0\pm1.4$ | 107 |
| 70 | $4.0\pm0.8$ | $4.5\pm0.9$ | $5.2\pm1.5$ | 107 |

[a] CN—average coordination number. The cutoff distance (in Å) used in the calculation of CN is shown in parentheses.
[b] The average bond angle using a 2.5 Å cut off distance for the determination of coordination.

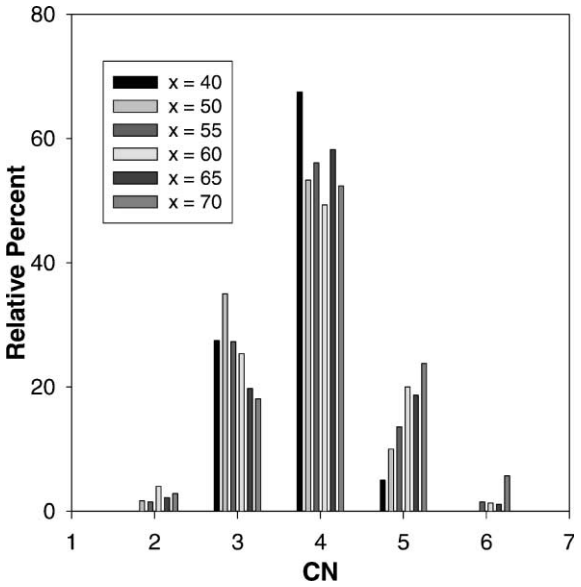


Fig. 7. Histogram plot of the distribution of CNs for the zinc atoms in the simulations cells for all of the compositions studied.

### 3.5. Medium range order of the Zn phosphate glass series $xZnO \cdot (100 - x)P_2O_5$

Fig. 8 shows the simulated glass structure at $x = 50$, 60, and 70 mol% ZnO. From these snapshots, the glass structure can be seen transitioning from long chains and some rings at the metaphosphate composition to that of isolated $PO_4$ tetrahedra within the pyrophosphate region.

## 4. Discussion

This paper describes use of MD simulations to understand and predict the structural and physical properties of a binary zinc phosphate glass series, $x\mathrm{ZnO}\cdot(100 - x)\mathrm{P_2O_5}$, $(40 \leqslant x \leqslant 70)$ where $x$ is the mole percent modifier. The correspondence between the simulated and experimental densities reported in the present paper is very similar to that observed for the MD simulations of the Na ultraphosphate glass series (Liang et al., unpublished results). It was noted, however, that the MD simulated densities deviate slightly from experimental values with increasing Zn concentration. One possibility for this deviation is the inadequate parameterization of the Zn–O interactions at higher Zn concentrations within the forcefield model. Another possibility is that the conditions (cell size and quench rate) under which the MD simulations were performed may have a major impact on the resulting densities.

In a recent paper by Huff et al. it was demonstrated that the choice of forcefield parameters, the number of atoms in the simulations, and the effective quench rate all effect the resulting MD simulations in vitreous silica [50]. In that study it was shown that for MD simulations using a smaller number of atoms within the cell (~650 atoms), that variations in the density were on the order of 5%, while for simulations using a larger number of atoms (~3000 atoms) the variations in the calculated densities were reduced to ~1% [50]. No major changes in the overall silica structure were observed for simulations of these different-sized cells. Variations in the quench rate were also noted to have distinct changes on the resulting structure, in particular, the CN distributions, as well as the resulting

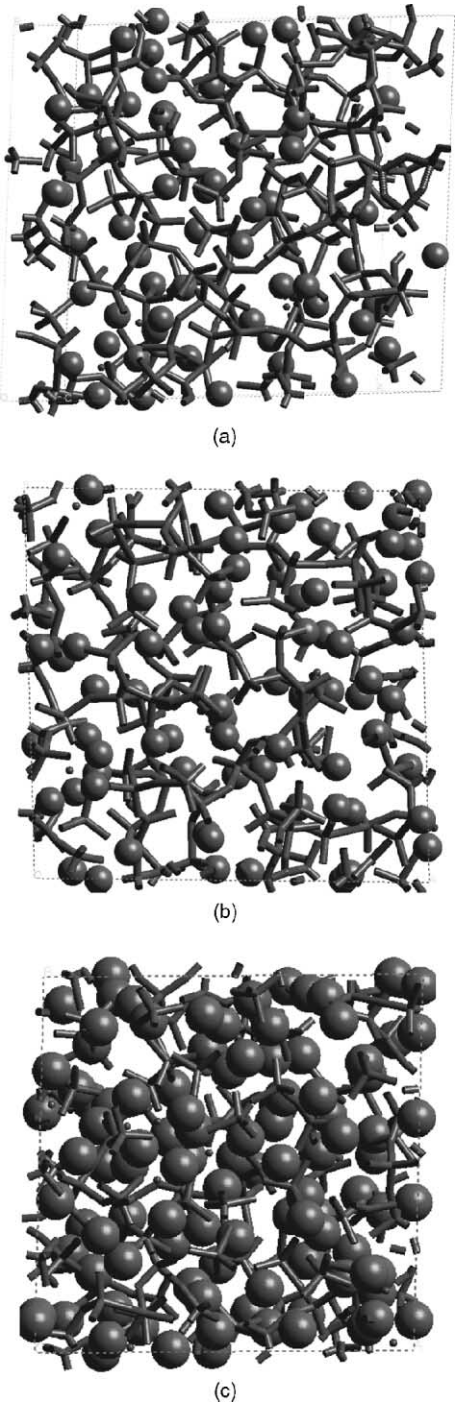


Fig. 8. Snapshots of the equilibrated simulation cell for glass compositions of (a) $50\mathrm{ZnO}\cdot 50\mathrm{P_2O_5}$, (b) $60\mathrm{ZnO}\cdot 40\mathrm{P_2O_5}$, and (c) $70\mathrm{ZnO}\cdot 30\mathrm{P_2O_5}$.

average density [50]. This shows that the slower quench rates allow the systems to reach an equilibrium position that is closer to that of the actual glass systems. If, however, error bars are associated with the data using the 5% error that was observed by Huff et al. for the effect of cell size, it can be seen that within this experimental error, there is no real difference between the different quench rates used for these systems (see Fig. 2). It also indicates that within the simulation variations there is no difference between the MD simulated and the experimental data points.

In addition, and following the findings of Huff et al., there was no observed change in the glass transition temperatures or the calculated radial distribution functions of these systems quenched at a slower rate for the $x = 50$ and 60 compositions of the zinc phosphate glass system. While there were no noticeable changes in glass transition temperatures with the simulated quench rate, the overall agreement is much better than that previously reported for the Li ultraphosphate glass MD simulations [24]. The agreement in the prediction of $T_g$ despite having an experimentally unrealistic quench rate, increases our confidence in the performance of this type of interatomic forcefield and molecular simulation, and the future ability to investigate more complex phosphate glass systems.

As shown above, there is good agreement between the simulations and the experimental data, but there are some distinct differences noted when the radial distribution functions are studied. The MD simulations reported here for the Zn phosphate glasses underestimate the P–O distance and distribution for the entire range of Zn compositions. A similar underestimation was noted in the MD analysis in the lithium metaphosphate glass [18]. It also appears that the MD simulations slightly overestimate the Zn–O distance for this series of glasses. While these differences are small, it does suggest that improvements to the forcefield model can be made for incorporation in future simulation studies. The majority of these improvements would most likely come from further studies of the crystal systems to provide increased accuracy of the atomic positions in each crystal. The intensity differences between the experimental and calculated plots shown in Fig. 5 are due to limitations in the software used to calculate the radial distribution functions from the neutron data to take into account the scattering efficiency of the atoms within the glass.

In phosphate glass systems the initial decrease in $T_g$ between the ultraphosphate composition ($x = 0$) and the metaphosphate composition ($x = 50$) is initially dominated by the reduction of phosphate tetrahedral crosslinking during the glass depolymerization with increasing modifier concentration. The ability of the polymer-like chains to twist and tangle after formation due to this loss of crosslinking is one of the possible explanations for the $T_g$ increase [51,52]. The structural variations that cause the increase in the $T_g$ between the Zn concentrations of $x = 50$ and 70 mol% are presently unknown. Analysis of the MD simulations shows that the Zn phosphate glass structure undergoes a significant long-range structural change with increasing zinc content, consistent with the reported experimental observations [15,48,53,54].

Recent investigations using double quantum magic angle spinning NMR, along with high resolution NMR techniques, has allowed the phosphate connectivity for these binary zinc phosphate glasses to be investigated [48,55]. It has been argued that the chains formed near the metaphosphate composition ($x = 50$) are responsible for the increase of $T_g$ up until that composition due to the structural stabilization produced by the entanglement of these phosphate chains similar to polymer systems. The MD simulations qualitatively support the argument of chain formation, as linear chains are clearly observed near the metaphosphate glass composition (see Fig. 8(a)). Unfortunately this explanation is not sufficient to explain the increasing $T_g$ behavior (Fig. 3) at higher Zn concentrations, where the continued break up of the phosphate chains to form isolated phosphate tetrahedra (Fig. 8(c)) is expected to decrease $T_g$.

At higher Zn concentrations the glass modifier within the system is also expected to play a more important role in the glass structure. Past work suggested that the coordinating zinc atoms in the glass structure begin to change from fourfold to fivefold as the glass composition approaches that of the orthophosphate [15,48], and could explain

the increasing $T_g$ above the metaphosphate composition. The average coordination of zinc in this study was found to be 4 although there was a broad distribution of CNs. A similar coordination environment was noted during the MD simulation of the $Zn(PO_3)_2$ glass [31]. The distribution of the O–Zn–O bond distance is also rather broad (not shown) with the most probable bond angle near 95°, also consistent with the results of Sourial et al. [31]. The average Zn–O bond distance of 1.98 Å, is very close to the average Zn–O distance of 1.97 Å of tetrahedrally coordinated zinc, and significantly different from the 2.06 Å of octahedrally coordinated zinc, based on crystal structures [45]. There are several studies that indicate a zinc CN of near 5 at the metaphosphate composition, while other work indicates that the CN is very dependent on preparation conditions and materials [12,19]. The presence of both fivefold- and sixfold-coordinated zinc has been shown to occur within the crystal systems of the binary zinc phosphates possibly due to these preparation dependencies [45,56]. While the structure of the crystal systems alone does not indicate that the same changes occur within the glass systems, other studies on zinc phosphate glasses have indicated that this coordination environment is possible [12,19]. Based on the present MD simulations it appears that the average coordination environment *does not* change over the Zn concentration range investigated, but the presence of non-tetrahedrally coordinated Zn does occur (see Fig. 7). This indicates that there is a need to look elsewhere for an explanation of the $T_g$ trends.

Our MD simulations, while reproducing the increasing $T_g$, do not support this argument that changes in the Zn CN are the dominant reason. In previous investigations of the lithium ultraphosphate glasses, it was shown that there was a correlation between the coordination of the P and Li and the change in $T_g$ behavior [18]. The average Zn CN of P (i.e. number of Zn around a given P) is shown in Table 5. This CN is expected to increase with increasing Zn concentration. In the MD analysis of the Li ultraphosphate glass system, a distinct discontinuity in the Li CN of P was noted at the $T_g$ minimum [18]. A similar change is not observed for the present MD investigation of the Zn phosphate glasses.

The average P CN of Zn (i.e. number of Zn around a given P) is shown in Table 5. Interestingly this number is invariant at ~4.6 for the entire Zn concentration range investigated. This CN would suggest that there is a lack of edge sharing phosphate tetrahedral present within the glass at any composition near or above the metaphosphate. The Zn atoms within the system have an average CN of 4 that is invariant throughout the composition range studied. The number of phosphate atoms within the secondary coordination sphere (within about 4 Å around each zinc atom, however, continually increases as more zinc is added to the system. It is possible that this preference of the Zn to link together as many as possible phosphate tetrahedral leads to the steady increase in the $T_g$ above the metaphosphate composition. This continues until approximately 75 mol% zinc at which time the $T_g$ once again drops. At this point there are no free oxygen atoms left for the zinc to bond to and the excess Zn must start to form a network of ZnO within the glass once again destabilizing the structure.

## 5. Conclusions

Using known crystal structures, an accurate energy forcefield model was developed for use with the binary zinc phosphate glass system, $x\mathrm{ZnO}\cdot(100-x)\mathrm{P_2O_5}$ $(40 < x < 70)$. Due to the special design of the model, it is expected to be useful for studying more complex glass compositions with desirable properties. The structure, glass transition temperature, and density of the glass compositions were calculated and compared to published data. There is very good agreement between the data, in spite of the large difference in quench rates between the simulations and the experimental data. Lowering the quench rate of the material was found to have a small positive effect on our MD simulations that allowed for an increase in the accuracy of the data. The simulations incorporate a forcefield model that takes into account the relatively short-range LJ interactions, long-range Coulombic interactions, and the energetics of the phosphorous–oxygen bond angles in the glass system. This study should provide a

sound atomistic basis for future model development that can be used to study more complex phosphate glass systems.

## Acknowledgements

Financial support of J.U.O.'s research from the US National Science Foundation (DMR9733350) is gratefully acknowledged. Financial support from the Basic Energy Science program at Sandia National Laboratories is also acknowledged. In addition, some of the work (B.C.T.) was performed as part of Sandia's Student Internship Program. Sandia is a multiprogram laboratory operated by the Sandia Corporation, a Lockheed Martin Company, for the United States Department of Energy under contract DE-AC04-94AL85000. Also, thanks are due to Jian-Jie Liang (SNL) for assistance in use of the MD simulation software, and to Chun Loong and Jackie Johnson (Argonne National Laboratory) for experimental assistance in acquisition of part of the neutron scattering data.

## References

[1] J.R. Van Wazer, Phosphorous and its Compounds, Interscience, New York, 1958.
[2] Y. Abe, J. Curley-Joseph, J. Feder, T.O. Henderson, R.L. Hilderbrand, H.R. Hudson, H.J. Lubansky, in: Topics in Phosphorus Chemistry, vol. 11, 1983.
[3] J.U. Otaigbe, G.H. Beall, Trends Polym. Sci. (Cambridge, UK) 5 (1997) 369.
[4] M. Ouchetto, B. Elouadi, S. Parke, Phys. Chem. Glasses 32 (1991) 8.
[5] B.J. Allan, B.V. Hiremath (Eds.), Solid State Optical Materials, vol. 28, American Ceramic Society, Westerville, OH, 1992.
[6] C.J. Quinn, P.D. Frayer, G.H. Beall, in: J.C. Salamone (Ed.), Polymeric Materials Encyclopedia, vol. 4, CRC, 1996.
[7] A. Musinu, G. Piccaluga, G. Pinna, D. Narducci, S. Pizzini, J. Non-Cryst. Solids 111 (1989) 221.
[8] P.M.T. Averbuch-Pouchot, A. Durif, M. Bagieu-Beucher, Acta Crystallogr. C 39 (1983) 25.
[9] A. Lai, A. Musinu, G. Piccaluga, S. Puligheddu, Phys. Chem. Glasses 38 (1997) 173.
[10] R.K. Brow, J. Non-Cryst. Solids 194 (1996) 267.
[11] E.C. Onyiriuka, J. Non-Cryst. Solids 163 (1993) 268.
[12] A. Musinu, G. Piccaluga, G. Pinna, G. Vlaic, D. Narducci, S. Pizzini, J. Non-Cryst. Solids 136 (1991) 198.
[13] R.K. Brow, D.R. Tallant, S.T. Myers, C.C. Phifer, J. Non-Cryst. Solids 191 (1995) 45.
[14] K. Meyer, J. Non-Cryst. Solids 209 (1997) 227.
[15] J.W. Wiench, M. Pruski, B. Tischendorf, J.U. Otaigbe, B.C. Sales, J. Non-Cryst. Solids 263&264 (2000) 101.
[16] M. Feike, C. Jäger, H.W. Spiess, J. Non-Cryst. Solids 223 (1998) 200.
[17] H. Eckert, Prog. NMR Spectrosc. 24 (1992) 159.
[18] T.M. Alam, J.-J. Liang, R.T. Cygan, Phys. Chem. Chem. Phys. 2 (2000) 4427.
[19] M. Bionducci, G. Licheri, A. Musini, G. Navarra, G. Piccaluga, G. Pinna, Z. Naturforsch., A 51 (1996) 1209.
[20] G.G. Boiko, N.S. Andreev, A.V. Parkachev, J. Non-Cryst. Solids 238 (1998) 175.
[21] G.G. Boiko, N.S. Andreev, A.V. Parkachev, Glass Phys. Chem. 24 (1998) 415.
[22] G. Cormier, J.A. Capobianco, A. Monteil, J. Non-Cryst. Solids 168 (1994) 115.
[23] A. Karthikeyan, P. Vinatier, A. Levasseur, K.J. Rao, J. Phys. Chem. B 103 (1999) 6185.
[24] J.J. Liang, R.T. Cygan, T.M. Alam, J. Non-Cryst. Solids 263&264 (2000) 167.
[25] L. Murawski, R.J. Barczynski, A. Rybicka, Proc. SPIE-Int. Soc. Opt. Eng. 3181 (1997) 136.
[26] K. Parlinski, H. Grimm, Phys. Rev. B 33 (1986) 4868.
[27] K. Parlinski, H. Grimm, Ferroelectrics 79 (1988) 331.
[28] A.G. Shikerkar, Solid State Phys., Proc. DAE Solid State Phys. Symp. 42nd (2000) 107.
[29] K. Shoji, I. Yasui, J. Non-Cryst. Solids 177 (1994) 125.
[30] R.K. Sistla, M. Seshasayee, Solid State Commun. 113 (1999) 35.
[31] E. Sourial, T. Peres, J.A. Capobianco, A. Speghini, M. Bettinelli, Phys. Chem. Chem. Phys. 1 (1999) 2013.
[32] A. Speghini, E. Sourial, T. Peres, G. Pinna, M. Bettinelli, J.A. Capobianco, Phys. Chem. Chem. Phys. 1 (1999) 173.
[33] T. Uchino, T. Yoko, J. Non-Cryst. Solids 263&264 (2000) 180.
[34] D.K. Belashchenko, Inorg. Mater. 33 (1997) 565.
[35] H. Inoue, A. Makishina, T. Kanazawa, T. Nanba, I. Yasui, Phys. Chem. Glasses 36 (1995) 37.
[36] M. Jansen, B. Luer, Acta Crystallogr. 177 (1986) 149.
[37] E.H. Arbib, B. Elouadi, J. Solid State Chem. 127 (1996) 350.
[38] D. Stachel, I. Svoboda, H. Fuess, Acta Crystallogr. C 51 (1995) 1049.
[39] C. Calvo, J. Phys. Chem. Solids 24 (1963) 141.
[40] C. Calvo, Can. J. Chem. 43 (1965) 436.
[41] C. Baez-Doelle, D. Stachel, Z. Kristallogr. 203 (1993) 232.
[42] B.E. Robertson, C. Calvo, J. Solid State Chem. 1 (1970) 120.
[43] J.S. Stephens, C. Calvo, Can. J. Chem. 45 (1967) 2303.

[44] A.G. Nord, T. Stefanidis, Mater. Res. Bull. 16 (1981) 1121.
[45] A.G. Nord, P. Kierkegaard, Chem. Scr. 15 (1980) 27.
[46] J.D. Gale, Royal Institiution of Great Britain/Imperial College, 1992–1994.
[47] OFF Energy Program ed.; Accelrys INC., 2001.
[48] B. Tischendorf, J.U. Otaigbe, J.W. Wiench, M. Pruski, B.C. Sales, J. Non-Cryst. Solids 282 (2001) 147.
[49] J.U. Otaigbe, C.K. Loong, et al., unpublished neutron diffraction data.
[50] N.T. Huff, E. Demiralp, T. Çagin, W.A. Goddard III, J. Non-Cryst. Solids 253 (1999) 133.
[51] N.H. Ray, Inorganic Polymers, Academic Press, New York, 1978.
[52] C.E. Crowder, J.U. Otaigbe, M.A. Barger, R.L. Sammler, B.C. Monahan, C.J. Quinn, J. Non-Cryst. Solids 210 (1997) 209.
[53] M. Feike, C. Jager, H.W. Spiess, J. Non-Cryst. Solids 223 (1998) 200.
[54] C. Jäger, P. Hartmann, R. Witter, M. Braun, J. Non-Cryst. Solids 263&264 (2000) 61.
[55] J.W. Wiench, B. Tischendorf, J.U. Otaigbe, M. Pruski, J. Molec. Struct. 602&603 (2002) 145.
[56] C. Calvo, Mater. Res. Bull. 16 (1981) 1121.